# First Results from the Taiwan Axion Search Experiment with Haloscope in the $19.47$–$19.84\,\mu\text{eV}$ Mass Range[*]

Ann Author[†] and Second Author[‡]

*Authors' institution and/or address*

*This line break forced with \\*

(TASEH Collaboration)

(Dated: February 16, 2022)

# Abstract

This paper presents the first results from the Taiwan Axion Search Experiment with Haloscope, a search for axions using a microwave cavity at frequencies between 4.707506 and 4.798145 GHz. Apart from the external signals from the instruments, no candidates with a significance more than $3.355\sigma$ were found. The experiment excludes models with the axion-two-photon coupling $|g_{a\gamma\gamma}| \gtrsim 7.7 \times 10^{-14}\,\mathrm{GeV}^{-1}$, a factor of ten above the benchmark KSVZ model for the mass range $19.47 < m_a < 19.84\,\mu\mathrm{eV}$. For the first time, constraints on the $|g_{a\gamma\gamma}|$ are placed in this mass region.

## CONTENTS

* A footnote to the article title

† Also at Physics Department, XYZ University.

‡ Second.Author@institution.edu

## I. INTRODUCTION

The axion is a hypothetical particle predicted as a consequence of a solution to the strong CP problem [1–3], i.e. why the CP symmetry is conserved in the strong interactions when there is an explicit CP-violating term in the QCD Lagrangian. In other words, why is the electric dipole moment of the neutron so tiny: $|d_n| < 1.8 \times 10^{-26} \ e \cdot \mathrm{cm}$ [4, 5]? The solution proposed by Peccei and Quinn is to introduce a new global Peccei-Quinn $\mathrm{U(1)_{PQ}}$ symmetry that is spontaneously broken; the axion is the pseudo Nambu-Goldstone boson of $\mathrm{U(1)_{PQ}}$ [1]. Axions are abundantly produced during the QCD phase transition in the early universe and may constitute the dark matter (DM). In the post-inflationary PQ symmetry breaking scenario, where the PQ symmetry is broken after inflation, current calculations suggest a mass range of 1—100 $\mu$eV for axions so that the cosmic axion density does not exceed the observed cold DM density [6–18]. Therefore, axions are compelling because they may explain at the same time puzzles that are on scales different by more than thirty orders of magnitude.

Axions could be detected and studied via their two-photon interaction, the so-called "inverse Primakoff effect". For QCD axions, i.e. the axions proposed to solve the strong CP problem, the axion-two-photon coupling constant $g_{a\gamma\gamma}$ is related to the mass of the axion $m_a$:

$$g_{a\gamma\gamma} = \left( \frac{g_\gamma \alpha}{\pi \Lambda^2} \right) m_a, \tag{1}$$

where $g_\gamma$ is a dimensionless model-dependent parameter, $\alpha$ is the fine-structure constant, $\Lambda = 78$ MeV is a scale parameter that can be derived from the mass and the decay constant of the pion, and the ratio of the up to down quark masses. The numerical values of $g_\gamma$ are -0.97 and 0.36 in the Kim-Shifman-Vainshtein-Zakharov (KSVZ) [19, 20] and the Dine-Fischler-Srednicki-Zhitnitsky (DFSZ) [21, 22] benchmark models, respectively.

The detectors with the best sensitivities to axions with a mass of $\approx \mu$eV, as first put forward by Sikivie [23, 24], are haloscopes consisting of a microwave cavity immersed in a strong

static magnetic field and operated at a cryogenic temperature. In the presence of an external magnetic field, the ambient oscillating axion field drives the cavity and they resonate when the frequencies of the electromagnetic modes in the cavity match the microwave frequency $f$, where $f$ is set by the total energy of the axion: $hf = E_a = m_a c^2 + \frac{1}{2} m_a v^2$; the signal power is further delivered to the readout probe followed by a low-noise linear amplifier. The axion mass is unknown, therefore, the cavity resonator must allow the possibility to be tuned through a range of possible axion masses. The Axion Dark Matter eXperiment (ADMX), one of the flagship dark matter search experiments, had developed and improved the cavity design and readout electronics over the years. The results from the previous versions of ADMX and the Generation 2 ADMX (ADMX G2) excluded the KSVZ benchmark model within the mass range of 1.9–4.2 $\mu$eV and the DFSZ benchmark model for the mass ranges of 2.66–3.31 and 3.9–4.1 $\mu$eV, respectively [25–31]. One of the major goals of ADMX G2 is to search for higher-mass axions in the range of 4–40 $\mu$eV (1–10 GHz), similarly for the axion experiments that were established during the last ten years. The Haloscope at Yale Sensitive to Axion Cold dark matter (HAYSTAC) had performed searches first for the mass range of 23.15–24 $\mu$eV and later at around 17 $\mu$eV; they excluded axions with $|g_\gamma| \geq 1.38 \, |g_\gamma|^{\text{KSVZ}}$ for $m_a = 16.96 - 17.12$ and 17.14–17.28 $\mu$eV, respectively [32]. The Center for Axion and Precision Physics Research (CAPP) constructed and ran simultaneously several experiments targeting at different frequencies; they have pushed the limits towards the KSVZ value within a narrow mass region of 10.7126–10.7186 $\mu$eV [33]. The QUest for AXions-$a\gamma$ (QUAX-$a\gamma$) also pushed their limits close to the upper bound of the QCD axion-two-photon couplings for $m_a \approx 43 \, \mu$eV [34].

This paper presents the first results and the analysis details of a search for axions for the mass range of 19.47–19.84 $\mu$eV, from the Taiwan Axion Search Experiment with Haloscope (TASEH). The expected axion signal power and signal line shape, the noise power, and the signal-to-noise ratio are described in Secs. I A–I B. An overview of the TASEH experimental setup is presented in Sec. II. Section III gives a brief description of the calibration for the whole amplification chain while Sec. IV details the analysis procedure. Section V presents the analysis of the synthetic axion data and Sec. VI discusses the systematic uncertainties that may affect the limits on the $|g_{a\gamma\gamma}|$. The final results and the conclusion are presented in Sec. VII and Sec. VIII, respectively.

## A. The expected axion signal power and signal line shape

The signal power extracted from a microwave cavity on resonance is given by:

$$P_s = \left( g_\gamma^2 \frac{\alpha^2 \hbar^3 c^3 \rho_a}{\pi^2 \Lambda^4} \right) \times \left( \omega_c \frac{1}{\mu_0} B_0^2 V C_{mnl} Q_L \frac{\beta}{1+\beta} \right), \tag{2}$$

where $\rho_a = 0.45$ GeV/cm$^3$ is the local dark-matter density. The second set of parentheses contains parameters related to the experimental setup: the angular resonant frequency of the cavity $\omega_c$, the vacuum permeability $\mu_0$, the nominal strength of the external magnetic field $B_0$, the volume of the cavity $V$, and the loaded quality factor of the cavity $Q_L = Q_0/(1+\beta)$, where $Q_0$ is the unloaded, intrinsic quality factor of the cavity and $\beta$ is the coupling coefficient which determines the amount of coupling of the signal to the receiver. The form factor $C_{mnl}$ is the normalized overlap of the electric field $\vec{E}$, for a particular cavity resonant mode, with the external magnetic field $\vec{B}$:

$$C_{mnl} = \frac{\left[ \int \left( \vec{B} \cdot \vec{E}_{mnl} \right) d^3 \boldsymbol{x} \right]^2}{B_0^2 V \int E_{mnl}^2 d^3 \boldsymbol{x}}. \tag{3}$$

Here, the magnetic field $\vec{B}$ points mostly along the axial direction ($z$-axis) of the cavity. The field strength has a small variation along the radial and axial directions and $B_0$ is the nominal magnetic field strength. For cylindrical cavities, the largest form factor is from the TM$_{010}$ mode. The expected signal power derived from the experimental parameters of TASEH (see Table I) is $P_s \simeq 1.5 \times 10^{-24}$ W for a KSVZ axion with a mass of $19.5\,\mu$eV.

In the direct dark matter search experiments, several assumptions were made in order to derive a signal line shape. The density and the velocity distributions of DM are related to each other through the gravitational potential. The DM in the galactic halo is assumed to be virialized. The DM halo density distribution is assumed to be spherically symmetric and close to be isothermal, which results in a velocity distribution similar to the Maxwell-Boltzmann distribution. The distribution of the measured signal frequency can be further derived from the velocity distribution after a change of variables and set $hf_a = m_a c^2$. Previous experimental results typically adopt the following function for frequency $f \geq f_a$:

$$\mathcal{F}(f) = \frac{2}{\sqrt{\pi}} \sqrt{f - f_a} \left( \frac{3}{\alpha} \right)^{3/2} e^{\frac{-3(f-f_a)}{\alpha}}, \tag{4}$$

where $\alpha \equiv f_a \langle v^2 \rangle / c^2$. For a Maxwell-Boltzmann velocity distribution, the variance $\langle v^2 \rangle$ and the most probable velocity (speed) $v_p$ are related to each other: $\langle v^2 \rangle = 3 v_p^2/2 = (270 \text{ km/s})^2$,

5

where $v_p = 220$ km/s is the local circular velocity of DM in the galactic rest frame. Equation (4) is modified if one considers that the relative velocity of the DM halo with respect to the Earth is not the same as the DM velocity in the galactic rest frame [35]. The velocity distributions shall also be truncated so that the DM velocity is not larger than the escape velocity of the Milky Way [36]. Several N-body simulations [37, 38] follow structure formation from the initial DM density perturbations to the largest halo today and take into account the merger history of the Milky Way, rather than assuming that the Milky Way is in a steady state; the simulated results suggest velocity distributions with more high-speed particles relative to the Maxwellian case [39, 40]. However, these numerical simulations contain only DM particles; an inclusion of baryons may enhance the halo's central density due to a condensation of gas towards the center of the halo via an adiabatic contraction [41, 42], or may reduce the density due to the supernova outflows, etc [43, 44].

In order to compare the results of TASEH with those of the former experiments, the analysis presented in this paper assumes an axion signal line shape by including Eq. (4) in the weights when merging the measured power from multiple frequency bins (see Sec. IV D). Still given the caveats above and a lack of strong evidence for any particular choice of the velocity distribution, the results without an assumption of signal line shape and the results with a simple Gaussian weight are also presented for comparison. In addition, a signal line width $\Delta f_a = m_a \langle v^2 \rangle / h \simeq 5$ kHz, which is much smaller than the TASEH cavity line width $f_a/Q_L \simeq 250$ kHz, is assumed and five frequency bins are merged to perform the final analysis. For a signal line shape as described in Eq. (4), a 5-kHz bandwidth includes about 95% of the distribution.

**B.    The expected noise and the signal-to-noise ratio**

Several physics processes can contribute to the total noise and all of them can be seen as Johnson thermal noise at some effective temperature, or the so-called system noise temperature $T_{\text{sys}}$. The total noise power in a bandwidth $b$ is then:

$$P_n = k_B T_{\text{sys}} b, \tag{5}$$

where $k_B$ is the Boltzmann constant. The system noise temperature $T_{\text{sys}}$ has three major components:

$$T_{\text{sys}} = T_{\text{b}} + T_{\text{qn}} + T_{\text{a}}, \tag{6}$$

where

$$T_{\text{qn}} = \frac{1}{2}\, hf/k_B\ . \tag{7}$$

The three terms in Eq. (6) correspond to the effective temperatures of the following noise sources: (i) $T_{\text{b}}$, the blackbody radiation from the cavity at a physical temperature $T_{\text{c}}$, (ii) $T_{\text{qn}}$, the quantum noise associated with the zero-point fluctuation of the vacuum, and (iii) $T_{\text{a}}$, the noise added by the receiver (mainly from the first-stage amplifier). Equation (6) implies that the noise spectrum has little dependence on the frequency (white spectrum) for the narrow bandwidth considered in the experiment. However, apart from the flat baseline as described by Eq. (6), the noise spectrum observed by TASEH has an additional component with a Lorentzian shape due to the higher temperature at the cavity with respect to the temperature in the DR. More details may be found in Sec. II and Appendix A. The Lorentzian component will be removed from the measured spectrum and only the baseline $T_{\text{sys}}$ will be used in the final analysis (Sec. IV).

Using the operation parameters of TASEH in Table I and the results from the calibration of readout electronics, the values of $T_{\text{b}}$, $T_{\text{qn}}$, and $T_{\text{a}}$ are estimated to be about 0.07 K, 0.12 K, and $1.9 - 2.2$ K, respectively. Therefore, the baseline value of $T_{\text{sys}}$ for TASEH is about 2.1–2.4 K, which gives a noise power of approximately $(1.5 - 1.7) \times 10^{-19}$ W within the 5-kHz axion signal line-width, three orders of magnitude larger than the signal. Nevertheless, what matters in the analysis is the signal significance, or the so-called signal-to-noise ratio (SNR) using the standard terminology of axion experiments, i.e. the ratio of the signal power to the fluctuation in the averaged noise power spectrum $\sigma_n$.

According to Dicke's Radiometer Equation [45], the $\sigma_n$ is given by:

$$\sigma_n = \frac{P_n}{\sqrt{N_{\text{avg}}}},$$

$$= \frac{P_n}{\sqrt{t\Delta f}},$$

$$= k_B T_{\text{sys}} \sqrt{\frac{\Delta f}{t}} \tag{8}$$

where $N_{\text{avg}}$ is the number of noise power spectra used in the average; it is related to the amount of data integration time $t$ and the bandwidth over which a single measurement is

7

made $\Delta f$. The SNR will therefore be:

$$\text{SNR} = \frac{P_s}{\sigma_n},$$

$$= \frac{P_s}{k_B T_{\text{sys}}} \sqrt{\frac{t}{\Delta f}}, \tag{9}$$

Combining Eq. (2) and Eq. (9), one could see that the SNR is maximized by an experimental setup with a strong magnetic field, a large cavity volume, an efficient cavity resonant mode, a receiver with low system noise temperature, and a long integration time.

## II. EXPERIMENTAL SETUP

The detector of TASEH is located at the Department of Physics, National Central University, Taiwan and housed within a cryogen-free dilution refrigerator (DR) from BlueFors. An 8-Tesla superconducting solenoid with a bore diameter of 76 mm and a length of 240 mm is integrated with the DR.

The data for the analysis presented in this paper were collected by TASEH from October 13, 2021 to November 15, 2021, and termed as the CD102 data, where CD stands for "cool down". During the data taking, the cavity sat in the center of the magnet bore and was connected via holders to the mixing flange of the DR at a temperature of $T_{\text{mx}} \approx 27$ mK. The temperature of the cavity stayed at $T_{\text{c}} \simeq 155$ mK, higher with respect to the DR; it is believed that the cavity had an accidental thermal contact with the radiation shield in the DR. The cavity, made of oxygen-free high-conductivity (OFHC) copper, has an effective volume of 0.234 L and is a two-cell cylinder split along the axial direction ($z$-axis). The cylindrical cavity has an inner radius of 2.5 cm and a height of 12 cm. In order to maintain a smooth surface, the cavity underwent the processes of annealing, polishing, and chemical cleaning. The resonant frequency of the $TM_{010}$ mode can be tuned over the range of 4.667–4.959 GHz via the rotation of an off-axis OFHC copper tuning rod, from the position closer to the cavity wall to the position closer to the cavity center (i.e. when the vector from the rotation axis to the tuning rod is at an angle of 0° to 180°, with respect to the vector from the cavity center to the rotation axis). The CD102 data cover the frequency range of 4.707506–4.798145 GHz. There were 839 resonant-frequency steps in total, with a frequency difference of $\Delta f_{\text{s}} = 95 - 115$ kHz between the steps. The value of $\Delta f_{\text{s}}$ was kept within 10% of 105 kHz rather than a fixed value, such that the rotation angle of the tuning rod

8

did not need to be fine-tuned and the operation time could be minimized; a 10% variation of the $\Delta f_\text{s}$ is found to have no impact on the $|g_{a\gamma\gamma}|$ limits. Each resonant-frequency step is denoted as a "scan" and the data integration time was about 32-42 minutes. The integration time was determined based on the target $|g_{a\gamma\gamma}|$ limits and the experimental parameters in Table I; the variation of the integration time aimed to remove the frequency-dependence in the $|g_{a\gamma\gamma}|$ limits caused by frequency dependence of the added noise $T_\text{a}$. The form factor $C_{010}$ as defined in Eq. (3) varies from 0.64 to 0.69 over the full frequency range. The intrinsic, unloaded quality factor $Q_0$ at the cryogenic temperature ($T_\text{c} \simeq 155$ mK) is $\simeq 60000$ at the frequency of 4.74 GHz.

An output probe, made of a 50-$\Omega$ semi-rigid coaxial cable that was soldered to an SMA (SubMiniature version A) connector, was inserted into the cavity and its depth was set for $\beta \simeq 2$. The signal from the output probe was directed to an impedance-matched amplification chain. The first-stage amplifier was a low noise high-electron-mobility transistor (HEMT) amplifier with an effective noise temperature of $\approx 2$ K, mounted on the 4K flange. The signal was further amplified at room temperature via a three-stage post-amplifier, and down-converted and demodulated to in-phase (I) and quadrature (Q) components and digitized by an analog-to-digital converter with a sampling rate of 2 MHz.

A more detailed description of the TASEH detector, the operation of the data run, and the calibration of the gain and added noise temperature of the whole amplification chain can be found in Ref. [46]. See Table I for the benchmark experimental parameters that can be used to estimate the sensitivity of TASEH.

## III.   CALIBRATION

The noise is one of the most important parameters for the axion searches. Therefore, calibration for the amplification chain is a crucial part in the operation of TASEH. In order to perform a calibration, the HEMT was connected to a heat source (a 50-$\Omega$ resistor) instead of the cavity; various values of input currents were sent to the source to change its temperature monitored by a thermometer. The power from the source was delivered following the same transmission line as that in the axion data running. The output power is fitted to a first-order polynomial, as a function of the source temperature, to extract the gain and added noise for the amplification chain. More details of the procedure can be found

TABLE I. The benchmark experimental parameters for estimating the sensitivity of TASEH. The definitions of the parameters can be found in Sec. I. More details regarding the determination and the measurements of some of the parameters may be found in Ref. [46].

| | |
|---|---|
| $f_{\mathrm{lo}}$ | 4.707506 GHz |
| $f_{\mathrm{hi}}$ | 4.798145 GHz |
| $N_{\mathrm{step}}$ | 839 |
| $\Delta f_{\mathrm{s}}$ | $95 - 115$ kHz |
| $B_0$ | 8 Tesla |
| $V$ | 0.234 L |
| $C_{010}$ | $0.64 - 0.69$ |
| $Q_0$ | $59000 - 65000$ |
| $\beta$ | $1.9 - 2.3$ |
| $T_{\mathrm{mx}}$ | 27–28 mK |
| $T_{\mathrm{c}}$ | 155 mK |
| $T_{\mathrm{a}}$ | $1.9 - 2.2$ K |
| $\Delta f_a$ | 5 kHz |

in Ref. [46].

The calibration was carried out before, during, and after the data taking, which showed that the performance of the system was stable over time. The average of the added noise $T_{\mathrm{a}}$ over 19 measurements has the lowest value of 1.9 K at the frequency of 4.8 GHz and the highest value of 2.2 K at 4.72 GHz, as presented in Fig. 1. The error bars are the RMS of $T_{\mathrm{a}}$ and the largest RMS is used to calculate the systematic uncertainty for the limits on $|g_{a\gamma\gamma}|$. The light blue points in Fig. 1 are the noise from the axion data estimated by removing the gain and subtracting the contribution from the cavity noise, assuming that the presence of a narrow signal in the data would have no effect on the estimation. A good agreement between the results from the calibration and the ones estimated from the axion data is shown. The biggest difference is 0.076 K in the frequency range during which the data were recorded after an earthquake. The source of the difference is not understood, therefore, the difference

10

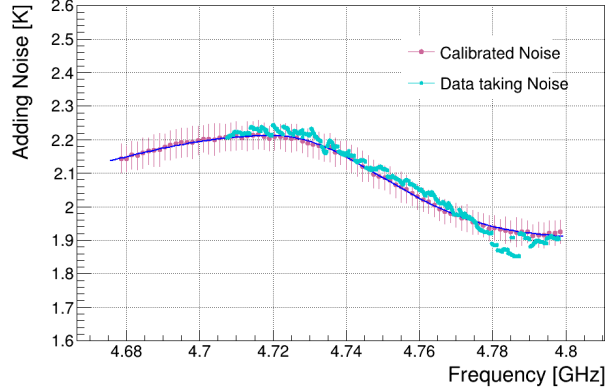is quoted as a systematic uncertainty together with the RMS of the noise.



FIG. 1. The average added noise obtained from the calibration (pink points) and the noise esti-mated from the axion data (light blue points) as a function of frequency. The error bars on the pink points are the RMS of the $T_a$, as computed from the 19 measurements for each frequency in the calibration. The blue curve is obtained after performing a fit to the pink points and is used to estimate the $T_a$ at each resonant frequency of the cavity.

## IV.   ANALYSIS PROCEDURE

The goal of TASEH is to find the axion signal hidden in the noise. In order to achieve this, the analysis procedure includes the following steps:

1. Perform fast Fourier transform (FFT) on the IQ time series data to obtain the frequency-domain power spectrum.

2. Apply the Savitzky-Golay (SG) filter to remove the structure of the background in the frequency-domain power spectrum.

3. Combine all power spectra from different frequency scans with the weighting algorithm.

4. Merge bins in the combined spectrum to maximize the SNR.

5. Rescan the frequency regions with candidates and set limits on the axion-two-photon coupling $|g_{a\gamma\gamma}|$ if no candidates were found.

11

The analysis is done by following the procedure similar to that adopted by the HAYSTAC experiment [47].

## A. Fast Fourier transform

The in-phase $I(t)$ and quadrature $Q(t)$ components of the time-domain data were sampled and saved in the TDMS (Technical Data Management Streaming) files - a binary format developed by National Instruments. The FFT is performed to convert the data into frequency-domain power spectrum in which the measured power is calculated using the following equation:

$$\text{Power} = \frac{|\text{FFT}(I + i \cdot Q)|^2}{N \cdot 2R}, \tag{10}$$

where $N$ is the number of data points ($N = 2000$ in the TASEH CD102 data), and $R$ is the input resistance of the signal analyzer (50 $\Omega$). The FFT is done for every one-millisecond subspectrum data. The integration time for each frequency scan was about 32-42 minutes, which resulted in 1920000 to 2520000 subspectra; an average over these subspectra gives the averaged frequency-domain power spectrum for each scan. The frequency span in the spectrum from each resonant-frequency scan is 1.6 MHz while the resolution is 1 kHz, giving 1600 frequency bins in each spectrum.

## B. Remove the structure of the background

In the absence of the axion signal, the output data spectrum is simply the noise from the cavity and the amplification chain. If axions are present in the cavity, the signal will be buried in the noise because the signal power is very weak. Therefore, the structure of the raw averaged output power spectrum, as shown in the upper panel Fig. 2, is dominated by the noise of the system and an explanation for the structure can be found in Appendix A. The Savitzky Golay (SG) filter [48], a digital filter that can smooth data without distorting the signal tendency, is applied to remove the structure of the background. The SG filter is performed on the averaged spectrum of each frequency scan by fitting adjacent points of successive sub-sets of data with an $n^{\text{th}}$-order polynomial. The result depends on two parameters: the number of data points used for fitting, the so-called window width, and the

12

order of the polynomial. If the window is too wide, the filter will not remove small structures, and if it is too narrow, it may kill the signal. The window and the order were first chosen during the data taking, by requiring the ratio of the raw data to the filter output consistent with unity. After the data taking, they were optimized by injecting an axion signal on top of the noise data and found that they were consistent with the original choice (see Sec. VI).

The raw averaged spectrum is divided by the output of the SG filter, then unity is subtracted from the ratio to get the normalized spectrum (lower panel of Fig. 2); if the axion signal exists, a power excess will be above zero. During the data taking, the resonant frequency of the cavity was adjusted by the tuning bar so to scan a large range of frequencies and to reduce the uncertainty of the averaged noise power at the overlapped region. Therefore, the spectra of all the scans need to be combined to create one big spectrum. Before doing this, the normalized spectrum from each scan is rescaled by $R_{ij}$, and the rescaled spectrum, shown in Fig. 3, is computed with the following formula:

$$\delta_{ij}^{\mathrm{res}} = R_{ij}\delta_{ij}^{\mathrm{norm}}, \tag{11}$$

and the standard deviation of each bin is:

$$\sigma_{ij}^{\mathrm{res}} = R_{ij}\sigma_i^{\mathrm{norm}}, \tag{12}$$

where

$$R_{ij} = \frac{k_B T_{\mathrm{sys}}\Delta f_{\mathrm{bin}}}{P_{ij}^{\mathrm{KSVZ}}h_{ij}}. \tag{13}$$

The $\delta_{ij}^{\mathrm{norm}}$ ($\delta_{ij}^{\mathrm{res}}$) and $\sigma_i^{\mathrm{norm}}$ ($\sigma_{ij}^{\mathrm{res}}$) are the normalized (rescaled) power and the standard deviation of the $j^{\mathrm{th}}$ frequency bin from the $i^{\mathrm{th}}$ resonant-frequency scan. The factor $R_{ij}$ is the ratio of the system noise power to the expected signal power of the KSVZ axion $P_{ij}^{\mathrm{KSVZ}}$, with the Lorentzian cavity response $h_{ij}$ taken into account. The system-noise temperature $T_{\mathrm{sys}}$ is calculated following Eq. (6), where the frequency dependence of the added-noise temperature $T_{\mathrm{a}}$ is obtained from the fitting function in Fig. 1. The $\Delta f_{\mathrm{bin}}$ is the bin width of spectrum (1 kHz). The $h_{ij} = \frac{1}{1+[2(f_{ij}-f_{ci})/\Delta f_{ci}]^2}$ describes the Lorentzian response of the cavity, where $\Delta f_{ci}$ is the cavity line width which depends on the resonant frequency $f_{ci}$ and the loaded quality factor. If a signal appears in a certain frequency bin $j$, its expected power will vary depending on the bin position due to the cavity's Lorentzian response. The rescaling will take into account this effect. The procedure of the normalization and the

13

rescaling also ensures that a KSVZ axion signal will have a power $\delta_{ij}^{\text{res}}$ that is approximately equal to unity.
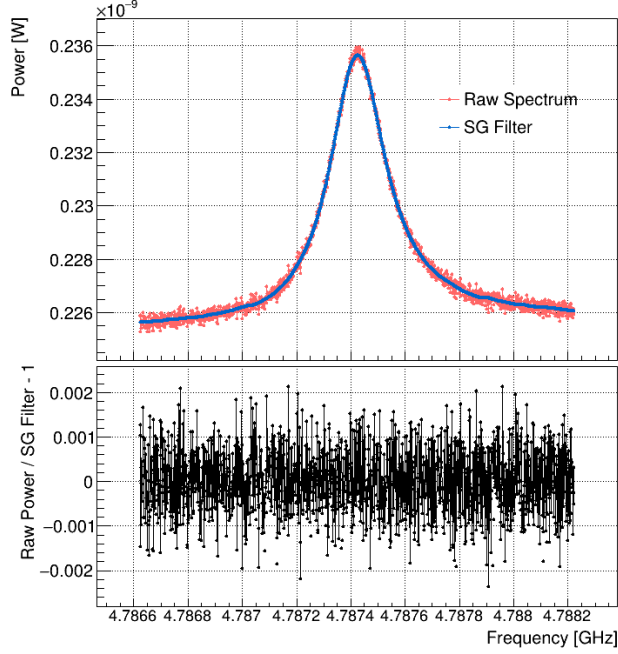


FIG. 2. Upper panel: The raw averaged power spectrum (red points) and the output of the SG filter (blue curve) of one scan. Lower panel: The normalized spectrum, derived by taking the ratio of the raw spectrum to the SG filter and subtracting unity from the ratio.

## C. Combine the spectra with the weighting algorithm

The purpose of the weighting algorithm is to add different spectra vertically, particularly for the frequency bins that appear in multiple spectra. Each spectrum was collected with a different cavity resonant frequency. Therefore, if a signal appears in a certain frequency bin $j$, due to the difference in the resonant frequency and the Lorentzian response, the expected signal power will be different in each spectrum $i$. The weighting algorithm is expected to take this into account with a weight calculated for each bin $j$ of the normalized and rescaled spectrum $i$, as defined in Eq. (14). The weighted power $\delta_n^{\text{com}}$ and the standard deviation $\sigma_n^{\text{com}}$ of the $n^{\text{th}}$ bin in the combined spectrum are calculated using Eq. (15) and Eq. (16), respectively. The SNR$_n^{\text{com}}$ is the ratio of $\delta_n^{\text{com}}$ to $\sigma_n^{\text{com}}$ as given in Eq. (17). Figure 4 and Fig. 5 show the power, the standard deviation, and the SNR of the combined spectrum,
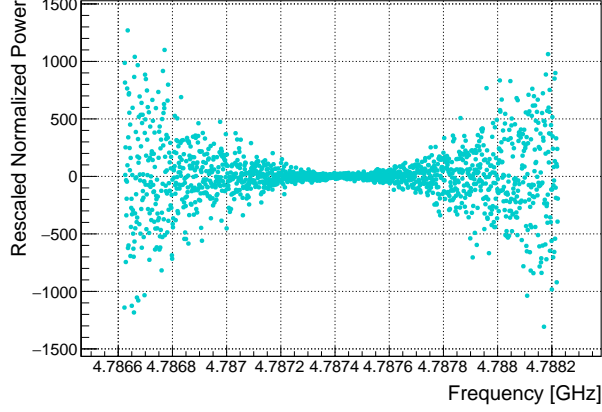
14

FIG. 3. The rescaled power spectrum, obtained by multiplying the normalized power with the ratio of the system noise power to the expected signal power of the KSVZ axion, with the Lorentzian response of the cavity taken into account.

respectively.

$$w_{ij} = \frac{1}{(\sigma_{ij}^{\text{res}})^2}, \tag{14}$$

$$\delta_n^{\text{com}} = \frac{\sum_1^k \left(\delta_{ij}^{\text{res}} \cdot w_{ij}\right)}{\sum_1^k w_{ij}}, \tag{15}$$

$$\sigma_n^{\text{com}} = \frac{\sqrt{\sum_1^k (\sigma_{ij}^{\text{res}} \cdot w_{ij})^2}}{\sum_1^k w_{ij}}, \tag{16}$$

$$\text{SNR}_n^{\text{com}} = \frac{\delta_n^{\text{com}}}{\sigma_n^{\text{com}}} = \frac{\sum_1^k \left(\delta_{ij}^{res} \cdot w_{ij}\right)}{\sqrt{\sum_1^k (\sigma_{ij}^{res} \cdot w_{ij})^2}}, \tag{17}$$

with $i$ running from 1 to $k$ where $k$ is the number of spectra that share the same frequency bin $j$.

## D. Merge bins

The expected axion bandwidth is about 5 kHz at the frequency of 5 GHz. In this paper, the interested frequency range is 4.707506– 4.798145 GHz and the bin width is 1 kHz. Therefore, in order to maximize the SNR, five consecutive bins with overlapping of the combined spectrum are merged to construct a final spectrum. The purpose of overlapping
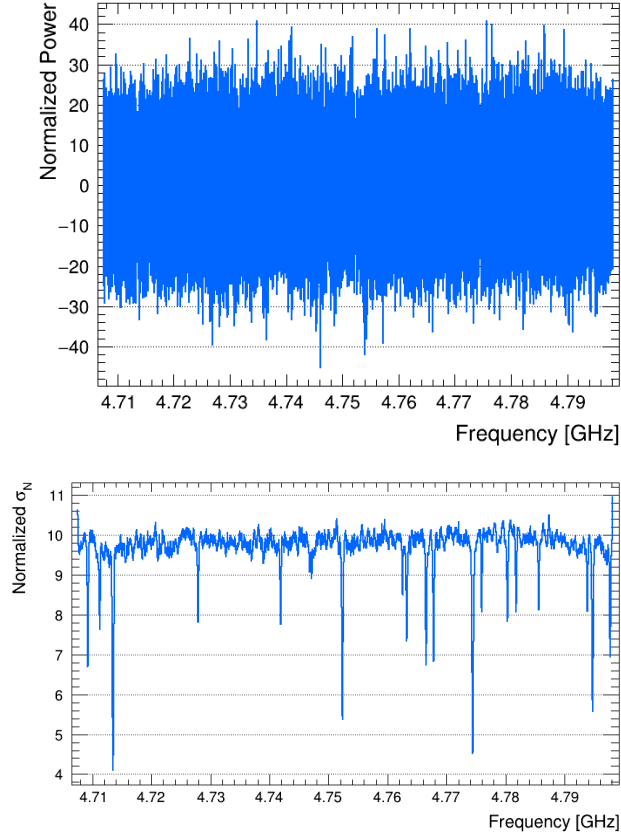
15

FIG. 4. The combined power $\delta$ following Eq. (15) (upper) and the standard deviation $\sigma$ derived from Eq. (16) (lower).
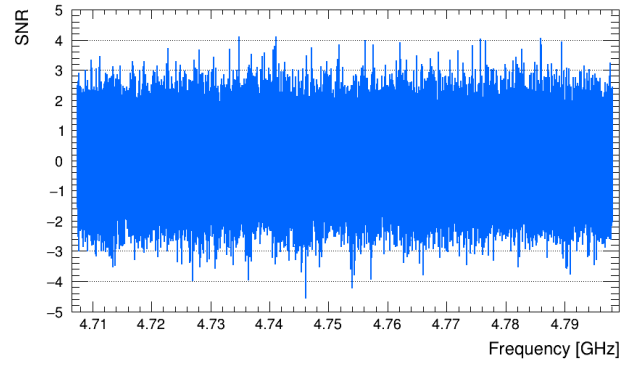


FIG. 5. The signal-to-noise ratio (SNR) calculated using Eq.(17) of the combined spectrum.

352 is to avoid the signal power broken into different neighboring bins of the merged spectrum.

353 Before defining the weights for merging, the power and the standard deviation of each bin

354 in the combined spectrum are multiplied with $M = 5$: $\delta_n^c \rightarrow M\delta_n^{\mathrm{com}}$ and $\sigma_n^c \rightarrow M\sigma_n^{\mathrm{com}}$. This

rescaling gives the expected mean of the normalized power $\mu_k^{\mathrm{com}} = 1$ if a KSVZ axion signal power leaves a fraction $1/M$ of its power in the $k^{\mathrm{th}}$ bin of the combined spectrum. Then the maximum likelihood weights, defined in Eq. (18) based on the Maxwellian line shape for axions [Eq. (4)], are used to build the merged spectrum.

$$w_n = \frac{L_n}{(\sigma_n^c)^2} = \frac{L_n}{(M\sigma_n^{\mathrm{com}})^2}, \tag{18}$$

where $M = 5$ is the number of merged bins, and

$$L_n = M \int_{f_a + \delta f_m + (n-1)\Delta f}^{f_a + \delta f_m + n\Delta f} \mathcal{F}(f)\,df, \tag{19}$$

where $n = 1, .., M$, $f_a = m_a c^2 / h$ is the axion frequency, $\delta f_m$ is the misalignment between $f_a$ and the lower bin boundaries in the combined spectrum and $\Delta f = 1$ kHz is the frequency bin width. The function $\mathcal{F}(f)$ has been defined in Eq. (4).

The power, the standard deviation and the SNR of the merged spectrum are:

$$\delta_g^{\mathrm{merged}} = \frac{\sum_{n=1}^{M}\left(\delta_{g+n-1}^c \cdot w_{g+n-1}\right)}{\sum_{n=1}^{M} w_{g+n-1}}, \tag{20}$$

$$\sigma_g^{\mathrm{merged}} = \frac{\sqrt{\sum_{n=1}^{M}\left(\sigma_{g+n-1}^c \cdot w_{g+n-1}\right)^2}}{\sum_{n=1}^{M} w_{g+n-1}}, \tag{21}$$

$$\mathrm{SNR}_g^{\mathrm{merged}} = \frac{\delta_g^{\mathrm{merged}}}{\sigma_g^{\mathrm{merged}}} = \frac{\sum_{n=1}^{M}\left(\delta_{g+n-1}^c \cdot w_{g+n-1}\right)}{\sqrt{\sum_{n=1}^{M}\left(\sigma_{g+n-1}^c \cdot w_{g+n-1}\right)^2}}, \tag{22}$$

where $g = 1, .., N - M + 1$ is the index for the frequency bins in the final spectrum. The total number of bins in the combined (final merged) spectrum is $N$ $(N - M + 1)$.

### E. Rescan and set limits on $|g_{a\gamma\gamma}|$

Before the collection of the CD102 data, a $5\sigma$ SNR target was chosen, which corresponds to a candidate threshold of $3.355\sigma$ at 95% confidence. After the merging as described in Sec. IV D, if there were any potential signal with an SNR larger than $3.355\sigma$, a rescan would be proceeded to check if it were a real signal or a statistical fluctuation. The procedure of the CD102 data taking was to perform a rescan after covering every 10 MHz; the rescan was done by adjusting the tuning rod of the cavity so to match the resonant frequency to the

17

frequency of the candidate. In total, 22 candidates with an SNR greater than $3.355\sigma$ were found. Among them, 17 candidates were from the fluctuations because they were gone after a few rescans. The remaining five candidates reached an SNR greater than $4\sigma$ after rescanning; a portable antenna outside the DR was used to probe if they came from external sources. The external signals in the frequency ranges of $4.710170 - 4.710190$ GHz and $4.747301 - 4.747380$ GHz from the instruments in the laboratory were detected, therefore, no limits are placed for these two ranges. More details can be found in the TASEH instrumentation paper [46]. Figure 6 and Fig. 7 show the power, the standard deviation, and the SNR of the merged spectrum after including data from both the original scans and the rescans, respectively.

Since no candidates were found after the rescan, an upper limit on the signal power $P_s$ is derived by setting $P_s$ equal to $5\sigma_q^{\mathrm{merged}}$ for a certain frequency bin $q$ in the merged spectrum. Then, the 95% C.L. limits on the dimensionless parameter $|g_\gamma|$ and the axion-two-photon coupling $|g_{a\gamma\gamma}|$ could be derived according to Eq. (2) and Eq. (1). See Sec. VII for the final limits including the systematic uncertainties.

## V. ANALYSIS OF THE SYNTHETIC AXION DATA

After TASEH finished collecting the CD102 data on November 15, 2021, the synthetic axion signals were injected into the cavity and read out via the same transmission line and amplification chain. The procedure to generate axion-like signals is summarized in Ref. [46]. Due to the uncertainties on the losses of readout electronics and transmission lines, the synthetic axion signals were not used to perform an absolute calibration of the search sensitivity. Instead, a test with synthetic axion signals could be used to verify the procedures of data acquisition and physics analysis. The signal-to-noise ratio (SNR) of the frequency bin with maximum power from the synthetic axion signals, at $4.708970$ GHz, was set to $\approx 3.35\sigma$, corresponding to a power of $\approx 6.03 \times 10^{-13}$ W in a 1-kHz frequency bin.

The same analysis procedure as described in Sec. IV was applied to the data with synthetic axion signals. Figure 8 presents the individual raw power spectra in 24 frequency scans. Before combining the 24 spectra vertically, the SNR of the maximum-power bin is measured to be $3.577\sigma$; the SNR is slightly higher than $3.35\sigma$ due to a 5% difference in the noise fluctuation between the measurements from the calibration and the measurements taken
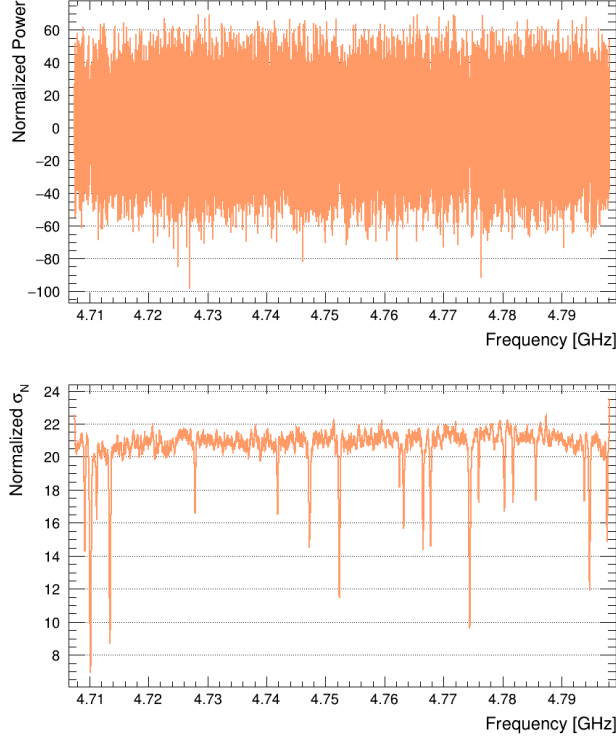
FIG. 6. The merged power $\delta$ following Eq. (20) (upper) and the standard deviation $\sigma$ derived from Eq. (21) (lower). The results shown were obtained using data from both the original scans and the rescans.
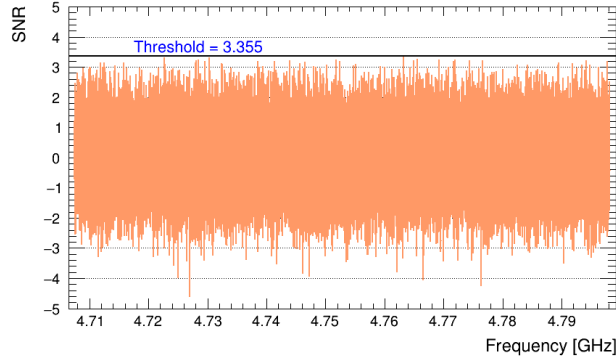


FIG. 7. The signal-to-noise ratio (SNR) calculated using Eq. (22) for the merged spectrum including data from both the original scans and the rescans. No candidate exceeds the threshold of $3.355\sigma$ (solid-black horizontal line).

408 right before injecting axion-like signals. After the vertical combination of power spectra
409 and the merging of five frequency bins, the SNRs increase to $4.74\sigma$ and $6.12\sigma$, respectively.

19

In addition to the injected synthetic axion signal, a candidate at 4.708006 GHz was found after merging the spectra. Since it was not possible to perform a rescan later, the real axion data from the two scans that had resonant frequencies close to the candidate frequency were added so to mimic the rescan; the candidate disappeared afterwards and is a statistical fluctuation. Figures 9– 10 present the spectra with the corresponding SNR, respectively, after combining the 24 spectra vertically and after merging five neighboring bins, including both the 24 scans of the synthetic axion data and the two scans of the real axion data. The analysis results of the synthetic axion signals prove that an power excess of more than $5\sigma$ can be found at the expected frequencies via the standard analysis procedure.
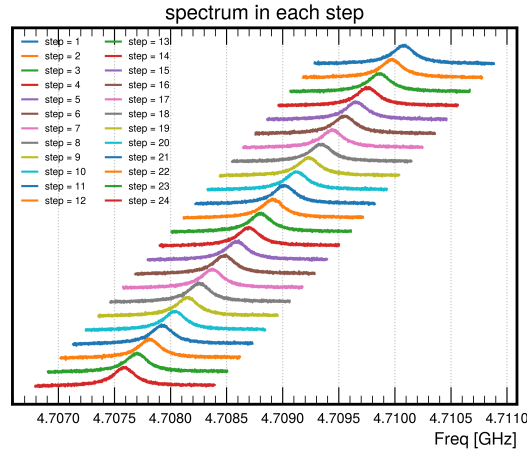


FIG. 8. The raw output power spectra, before applying the SG filter, from the 24 frequency steps of the synthetic axion data. In order to show the spectra clearly, the spectra are shifted with respect to each other with an arbitrary offset in the vertical scale.

## VI.   SYSTEMATIC UNCERTAINTIES

The systematic uncertainties on the $|g_{a\gamma\gamma}|$ limits arise from the following sources:

- Uncertainty on the product $Q_L \beta / (1 + \beta)$ in Eq. (2): In order to extract the loaded quality factor $Q_L$ and the coupling parameter $\beta$, a fitting of the measured results of the cavity scattering matrix was performed, which results in a relative uncertainty of 0.2% on this product.
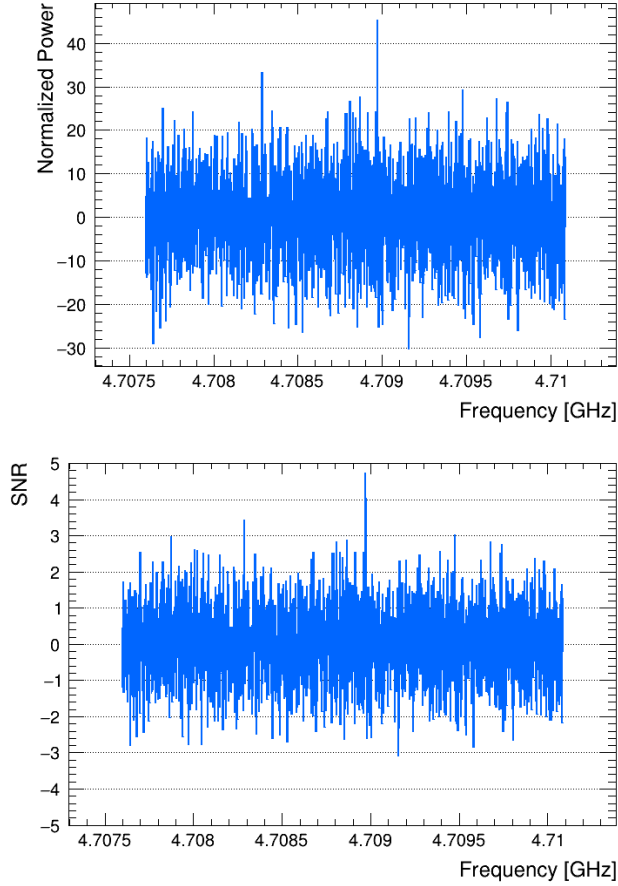
20

FIG. 9. The power (upper) and the signal-to-noise ratio (lower) after combining the spectra of the synthetic axion data with overlapping frequencies vertically. The procedure and the weights for combination are summarized in Sec. IV.

- Uncertainty on the noise temperature $T_\mathrm{a}$ from the RMS of the measurements in the calibration: $\Delta T_\mathrm{a}/T_\mathrm{a} = 2.3\%$ (see Sec. III and Fig. 1).

- Uncertainty on the noise temperature $T_\mathrm{a}$ from the largest difference between the value determined by the calibration and that from the axion data: $\Delta T_\mathrm{a}/T_\mathrm{a} = 4\%$ (see Sec. III and Fig. 1).

- Uncertainty from the choice of the SG-filter parameters: i.e. the window width and the order of the polynomial in the SG filter. At the beginning of the data taking, a preliminary optimization was performed: a window width of 201 bins and a $4^{\mathrm{th}}$ order polynomial were used for the first analysis of the CD102 data (see Sec. IV). This choice was kept for the central results. Nevertheless, various methods of optimization were
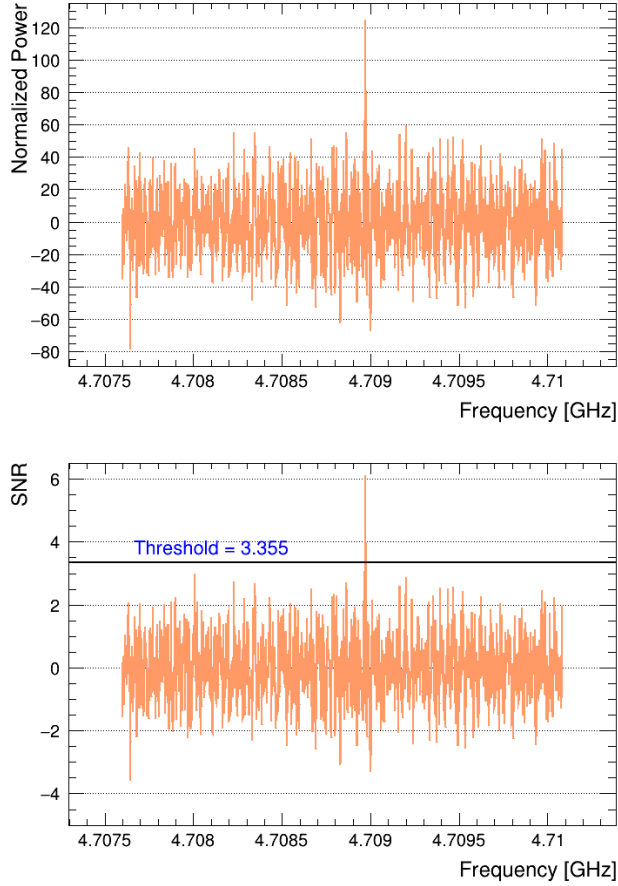
21

FIG. 10. The power (upper) and the signal-to-noise ratio (lower) after merging the power measured in five neighboring frequency bins of the synthetic axion data. The procedure and the weights for merging are summarized in Sec. IV.

439 also explored. The goal of the optimization is to find a set of SG-filter parameters that
440 only model the noise spectrum and do not remove a real signal. The methods include:

441     – Minimize the difference between the two functions returned by the SG filter, when
442     the SG filter is applied to: (i) the real data only, and (ii) the sum of the real data
443     and a simulated axion signal.

444     – Minimize the difference between the function returned by the SG filter and the
445     input noise function (including the Lorentzian distribution due to the cavity
446     noise), when the SG filter is applied to a spectrum that includes the simulation
447     of the axion signal and the simulation based on the input noise function. See
448     Fig. 11 for a comparison of the simulated spectrum, input noise function, and

22

the function returned by the SG filter when a $3^{\mathrm{rd}}$-order polynomial and a window of 141 bins are chosen; the differences from all the frequency bins are summed together when performing the optimization. Figure 12 shows the difference as a function of window widths when the order of polynomial is set to three, four, and six.

– Compare the mean $\mu_{\mathrm{noise}}$ and the width $\sigma_{\mathrm{noise}}$ of the measured power, assuming no signal is present in the data. See Fig. 13 for an example distribution of the measured power from the averaged spectrum of a single scan, when the cavity resonant frequency is 4.798147 GHz; a Gaussian fit is performed to extract $\mu_{\mathrm{noise}}$ and $\sigma_{\mathrm{noise}}$. Given the nature of the thermal noise, the two variables are supposed to be related to each other if proper window width and order are chosen:

$$\sigma_{\mathrm{noise}} = \frac{\mu_{\mathrm{noise}}}{\sqrt{N_{\mathrm{spectra}}}},$$

where $N_{\mathrm{spectra}}$ is the number of spectra for averaging and is related to the amount of integration time for each frequency step. In general, $N_{\mathrm{spectra}} = 1920000 - 2520000$.

In addition, one could choose to optimize for each frequency step individually, optimize for a certain frequency step but apply the results to all data, or optimize by adding all the frequency steps together. Figure 14 shows that the deviations from the central results using different optimization approaches are in general within 1% and the maximum deviation of 1.8% on the $|g_{a\gamma\gamma}|$ limit is used as a conservative estimate of the systematic uncertainty from the SG filter.

The first source of the systematic uncertainty has negligible effect on the limits of $|g_{a\gamma\gamma}|$ while the latter three sources are studied and added in quadrature to obtain the total systematic uncertainty. The systematic uncertainties on the $|g_{a\gamma\gamma}|$ limits are displayed together with the central results in Sec. VII. Overall the total relative systematic uncertainty is $\approx 3.4\%$.

## VII. RESULTS

Figure 15 shows the limits on the axion-two-photon coupling $|g_{a\gamma\gamma}|$ and the ratio of the limits on the dimensionless parameter $|g_{\gamma}|$ with respect to the KSVZ benchmark value
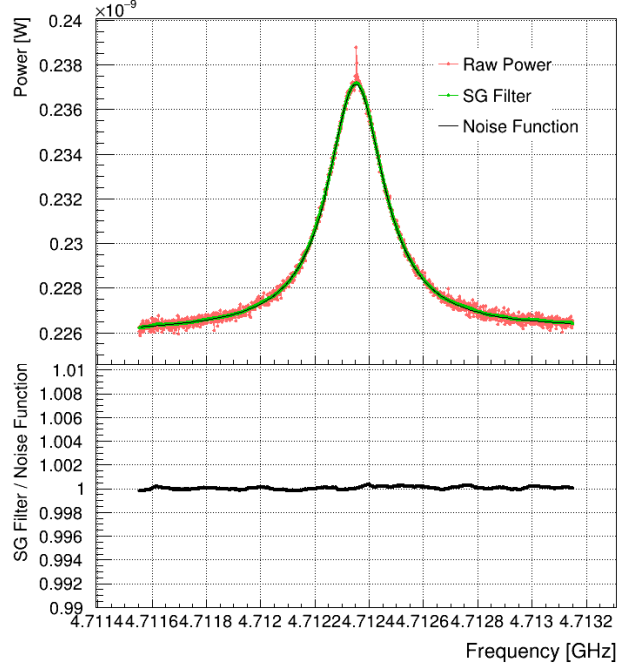
23

FIG. 11. Upper panel: The simulated spectrum, including the axion signal and the noise, is overlaid with the input noise function and the function returned by the SG filter. Lower panel: The ratio of the function returned by the SG filter to the input noise function.
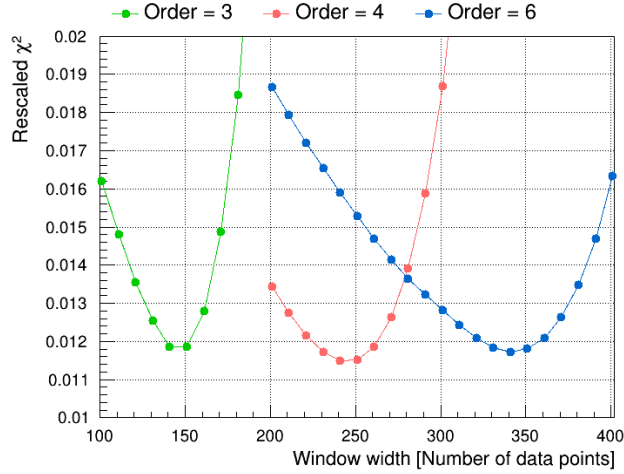


FIG. 12. The difference between the function returned by the SG filter and the input noise function, when various values of window widths and a $3^{\text{rd}}$, a $4^{\text{th}}$, or a $6^{\text{th}}$-order polynomial are applied in the SG filter. In this figure, the best choice is a $4^{\text{th}}$-order polynomial with a window width of 241 data points (bins).
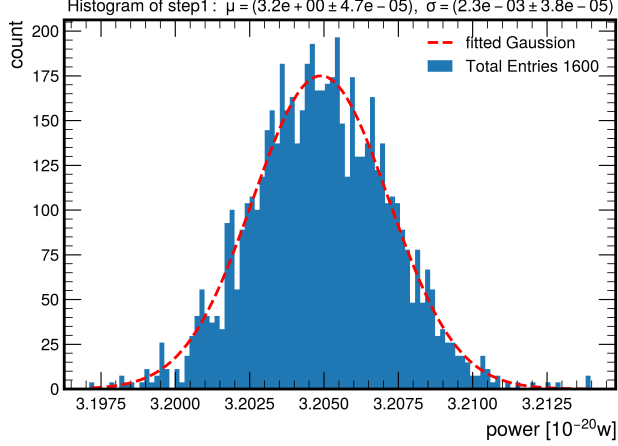
FIG. 13. An example of the distribution of the measured power, after removing the receiver gain and applying the SG filter, when the cavity resonant frequency is 4.798147 GHz. The distribution contains 1600 entries and each entry corresponds to the measured power in one frequency bin, averaged over 1920000 subspectra. The mean and the width returned by a Gaussian fit to the distribution are used to determine the best choice of SG parameters. The mean $\mu_{\text{noise}} = 3.2 \times 10^{-20}$ W in a 1-kHz frequency bin would imply a noise temperature of 2.3 K.

($|g_{\text{KSVZ}}| = 0.97$). The blue error band indicates the systematic uncertainties as discussed in Sec. VI. No limits are placed for the frequency ranges of $4.710170 - 4.710190$ GHz and $4.747301 - 4.747380$ GHz, which correspond to the external signal from the instruments in the laboratory during the collection of the CD102 data. The limits on $|g_{a\gamma\gamma}|$ range from $4.4 \times 10^{-14}$ to $8.3 \times 10^{-14}$, with an average value of $7.7 \times 10^{-14}$; the lowest value comes from the frequency bins with additional eight times more data from the rescans, while the highest value comes from the frequency bins near the boundaries of the spectrum. Figure 16 displays the limits on $|g_{a\gamma\gamma}|$ obtained by TASEH with those from the previous searches. The results of TASEH exclude the models with the axion-two-photon coupling $|g_{a\gamma\gamma}| \gtrsim 7.7 \times 10^{-14}\,\text{GeV}^{-1}$, a factor of ten above the benchmark KSVZ model for the mass range $19.47 < m_a < 19.84\,\mu\text{eV}$ (corresponding to the frequency range of $4.707506 < f_a < 4.798145$ GHz).

The central results shown in Figs. 15–16 were obtained assuming an axion signal line shape that follows Eq. (4). Both the analysis that merges bins without including a weight from the signal line shape [$L_n = 1$ in Eq. (18)] and the one that assumes a simple Gaussian weight, with a mean at the center of the five frequency bins and a width $\sigma$ giving half-maximum-
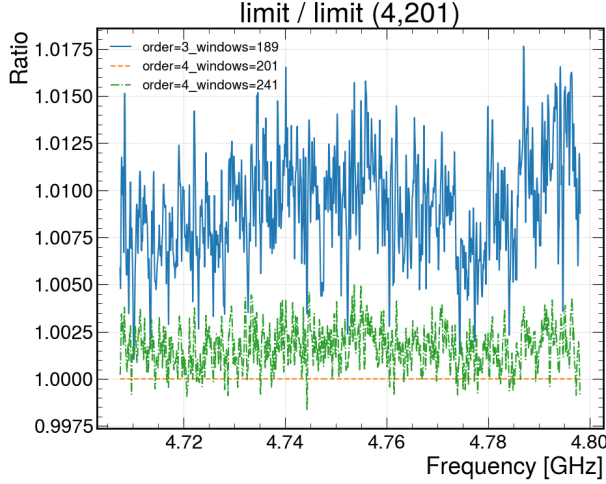
25

FIG. 14. The ratios of the limits on $|g_{a\gamma\gamma}|$ due to the different choices of the window width and the order of polynomial in the SG filter, with respect to the central results (a window width of 201 bins and the 4th-order polynomial). The window width of 241 bins and the 4th-order polynomial were obtained from the optimization after injecting an axion signal on top of a simulated noise spectrum. The window width of 189 bins and the 3rd-order polynomial were obtained from the optimization after comparing the means and the widths of the measured power distributions.

weight when the frequency is 2.5 kHz away from the center, i.e. $\sigma = 5\,\text{kHz}\Big/2\sqrt{2\ln 2}$, produce limits that are 5-6% higher than the central results (see Fig. 17).

## VIII. CONCLUSION

This paper presents the first results of a search for axions for the mass range $19.47 < m_a < 19.84\,\mu\text{eV}$, using the CD102 data collected by the Taiwan Axion Search Experiment with Haloscope from October 13, 2021 to November 15, 2021. Apart from the external signals, no candidates with a significance more than $3.355\sigma$ were found. The experiment excludes models with the axion-two-photon coupling $|g_{a\gamma\gamma}| \gtrsim 7.7 \times 10^{-14}\,\text{GeV}^{-1}$, a factor of ten above the benchmark KSVZ model. This is the first time that constraints on the $|g_{a\gamma\gamma}|$ are placed in this mass region. The synthetic axion signals were injected after the collection of data and the successful results validate the data acquisition and the analysis procedure.

The target of TASEH is to search for axions for the mass range of 16–40 $\mu$eV, corresponding to a frequency range of 3.9–9.7 GHz. In the coming years, several upgrades are expected,
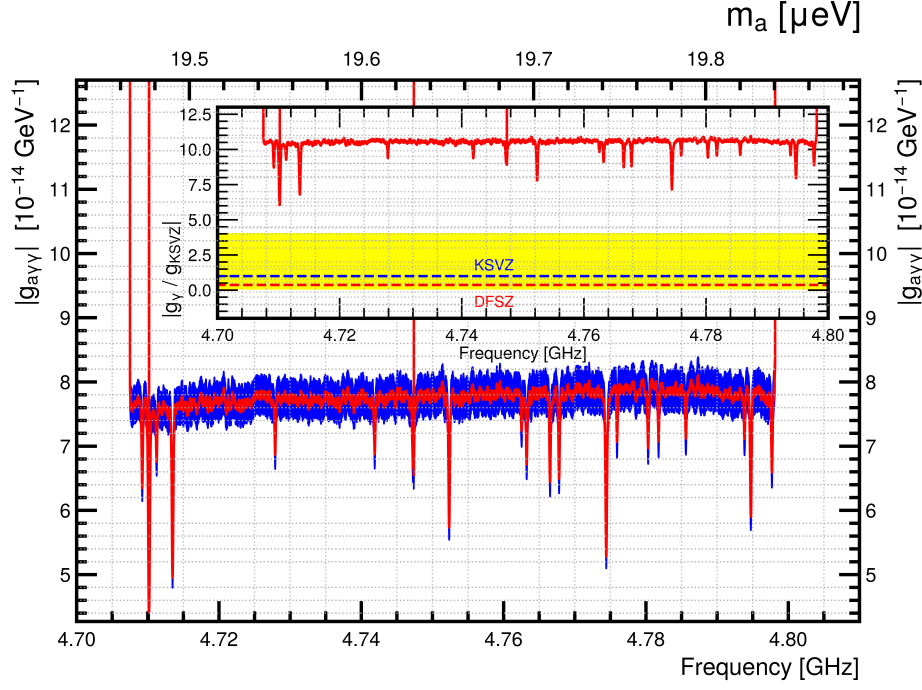
26

FIG. 15. The limits on $|g_{a\gamma\gamma}|$ and the ratio of the limits on $|g_\gamma|$ relative to $|g_{\mathrm{KSVZ}}| = 0.97$ (inset) for the frequency range of 4.707506–4.798145 GHz. The blue error band indicates the systematic uncertainties as discussed in Sec. VI. The yellow band in the inset shows the allowed region of $|g_\gamma|$ vs. $m_a$ from various QCD axion models, while the blue and red dashed lines are the values predicted by the KSVZ and DFSZ benchmark models, respectively

499 including: the use of the Josephson parametric amplifier as the first-stage amplifier, the re-
500 placement of the existing dilution refrigerator with a new one that has a magnetic field of
501 9 Tesla and a larger bore size, and the development of a new cavity with an effective volume
502 reaching one liter. These upgrades will reduce the added noise by a factor of 10 and increase
503 the magnetic field and the cavity volume by a factor of 1.125 and 5. With the improvements
504 of the experimental setup and several years of data taking, TASEH is expected to probe the
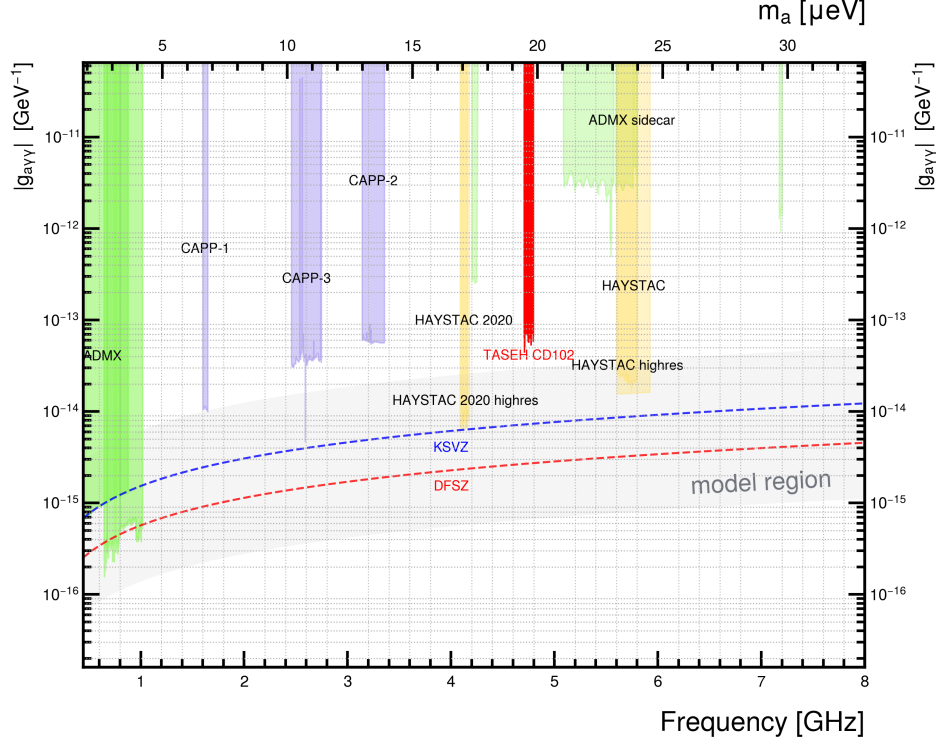505 QCD axion photon band in the target mass range.

FIG. 16. The limits on the axion-two-photon coupling $|g_{a\gamma\gamma}|$ for the frequency ranges of 0.4–8 GHz, from the CD102 data of TASEH and previous searches performed by the ADMX, CAPP, and HAYSTAC Collaborations. The gray band indicates the allowed region of $|g_{a\gamma\gamma}|$ vs. $m_a$ from various QCD axion models while the blue and red dashed lines are the values predicted by the KSVZ and DFSZ benchmark models, respectively.

**ACKNOWLEDGMENTS**

**Appendix A: The Derivation of the Noise Spectrum from the Cavity**

The Hamiltonian of a single-mode cavity is

$$H = \hbar\omega_{\mathrm{c}}(C^\dagger C + \frac{1}{2}), \tag{A1}$$

where $\omega_{\mathrm{c}}/2\pi$ is the cavity resonant frequency and $C$ is the annihilation operator of the inner cavity field. The cavity field is coupled to the modes $A$ of a transmission line with the rate $\kappa_2$. The cavity field is also coupled to the environment modes $B$ with the rate $\kappa_0$. Based on the model of Fig. 18 and the input-output theory, the equation of motion for $C$ is obtained:

$$\frac{dC}{dt} = -i\omega_{\mathrm{c}}C - \frac{\kappa_2 + \kappa_0}{2}C + \sqrt{\kappa_2}A_{\mathrm{in}} + \sqrt{\kappa_0}B_{\mathrm{in}}. \tag{A2}$$
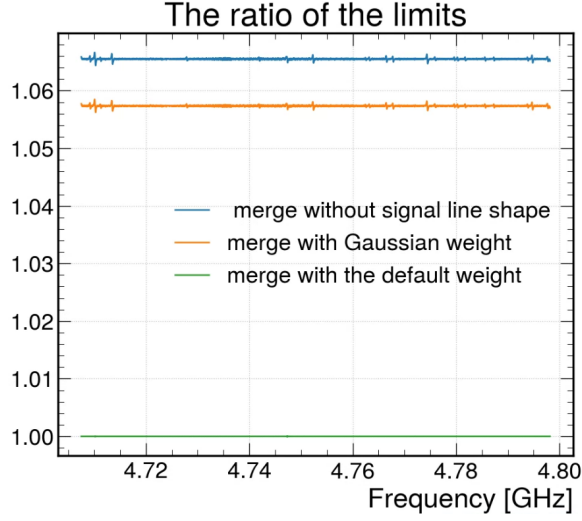
28

FIG. 17. The ratios of the limits on $|g_{a\gamma\gamma}|$ from the merging without assuming a signal line shape (blue) and from the merging with a Gaussian weight (orange), with respect to the central results.

A boundary condition holds for the transmission modes:

$$A_{\text{out}} = \sqrt{\kappa_2}C - A_{\text{in}}. \tag{A3}$$

Considering working in a rotating frame of the signal frequency $\omega$ near $\omega_c$, the equation of motion becomes:

$$-i\omega C + \frac{dC}{dt} = -i\omega_c C - \frac{\kappa_2 + \kappa_0}{2}C + \sqrt{\kappa_2}A_{\text{in}} + \sqrt{\kappa_0}B_{\text{in}}. \tag{A4}$$

The steady state solution for the cavity field is:

$$C = \frac{\sqrt{\kappa_2}A_{\text{in}} + \sqrt{\kappa_0}B_{\text{in}}}{-i(\omega - \omega_c) + \frac{\kappa_2 + \kappa_0}{2}}. \tag{A5}$$

By substituting Eq. (A5) into Eq. (A3), the reflected modes of the transmission line $A_{\text{out}}$ are expressed in terms of the input modes of the transmission line $A_{\text{in}}$ and the environment $B_{\text{in}}$:

$$
\begin{aligned}
A_{\text{out}} &= \frac{i(\omega - \omega_c) + \frac{\kappa_2 - \kappa_0}{2}}{-i(\omega - \omega_c) + \frac{\kappa_2 + \kappa_0}{2}}A_{\text{in}} + \frac{\sqrt{\kappa_2\kappa_0}}{-i(\omega - \omega_c) + \frac{\kappa_2 + \kappa_0}{2}}B_{\text{in}} \\
&= \frac{-(\omega - \omega_c)^2 + \frac{\kappa_2^2 - \kappa_0^2}{4} + i\kappa_2(\omega - \omega_c)}{(\omega - \omega_c)^2 + (\frac{\kappa_2 + \kappa_0}{2})^2}A_{\text{in}} \\
&\quad + \frac{\sqrt{\kappa_2\kappa_0}\frac{\kappa_2 + \kappa_0}{2} + i\sqrt{\kappa_2\kappa_0}(\omega - \omega_c)}{(\omega - \omega_c)^2 + (\frac{\kappa_2 + \kappa_0}{2})^2}B_{\text{in}}.
\end{aligned} \tag{A6}
$$

29

Therefore, the autocorrelation of $A_{\text{out}}$ is related to those of $A_{\text{in}}$ and $B_{\text{in}}$:

$$\langle A^{\dagger}_{\text{out}} A_{\text{out}} \rangle = \frac{[(\omega - \omega_c)^2 - \frac{\kappa_2^2 - \kappa_0^2}{4}]^2 + \kappa_2^2(\omega - \omega_c)^2}{[(\omega - \omega_c)^2 + (\frac{\kappa_2 + \kappa_0}{2})^2]^2} \langle A^{\dagger}_{\text{in}} A_{\text{in}} \rangle$$
$$+ \frac{\kappa_2 \kappa_0 (\frac{\kappa_2 + \kappa_0}{2})^2 + \kappa_2 \kappa_0 (\omega - \omega_c)^2}{[(\omega - \omega_c)^2 + (\frac{\kappa_2 + \kappa_0}{2})^2]^2} \langle B^{\dagger}_{\text{in}} B_{\text{in}} \rangle. \tag{A7}$$

The spectrum from the cavity $S(\omega)$ is found to be related to the spectrum of the readout transmission line $S_{\text{rt}}(\omega)$ and the spectrum of the cavity environment $S_{\text{cav}}(\omega)$:

$$S(\omega) = \frac{[(\omega - \omega_c)^2 - \frac{\kappa_2^2 - \kappa_0^2}{4}]^2 + \kappa_2^2(\omega - \omega_c)^2}{[(\omega - \omega_c)^2 + (\frac{\kappa_2 + \kappa_0}{2})^2]^2} S_{\text{rt}}(\omega)$$
$$+ \frac{\kappa_2 \kappa_0 (\frac{\kappa_2 + \kappa_0}{2})^2 + \kappa_2 \kappa_0 (\omega - \omega_c)^2}{[(\omega - \omega_c)^2 + (\frac{\kappa_2 + \kappa_0}{2})^2]^2} S_{\text{cav}}(\omega). \tag{A8}$$

As the the readout transmission line and the cavity environment are both in thermal states, i.e. $S_{\text{rt}}(\omega) = [n_{\text{BE}}(T_{\text{rt}}) + 1/2] \hbar\omega$ and $S_{\text{cav}}(\omega) = [n_{\text{BE}}(T_{\text{cav}}) + 1/2] \hbar\omega$, where $n_{\text{BE}}$ is the mean photon number given by the Bose-Einstein distribution, $S(\omega)$ is white if $T_{\text{cav}} = T_{\text{rt}}$, and Lorentzian if $T_{\text{cav}} \gg T_{\text{rt}}$.
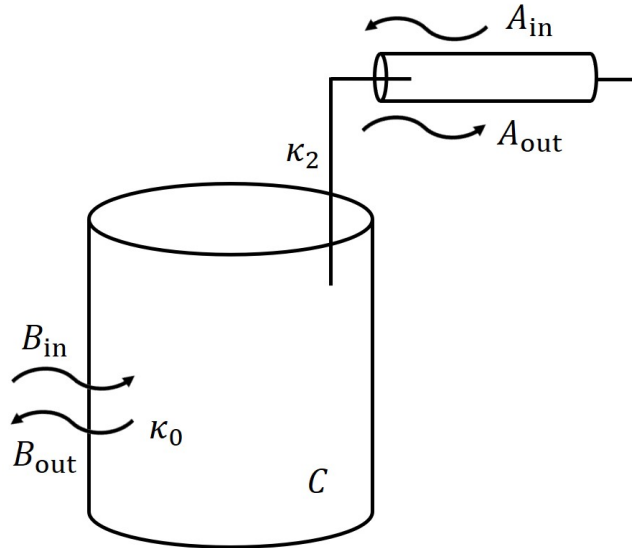


FIG. 18. A cavity is coupled to the modes of transmission line $A$ with the rate $\kappa_2$ and the modes of environment $B$ with the rate $\kappa_0$.

[1] R. D. Peccei and H. R. Quinn, CP conservation in the presence of pseudoparticles, Phys. Rev. Lett. **38**, 1440 (1977).

[2] S. Weinberg, A new light boson?, Phys. Rev. Lett. **40**, 223 (1978).

[3] F. Wilczek, Problem of strong $p$ and $t$ invariance in the presence of instantons, Phys. Rev. Lett. **40**, 279 (1978).

[4] C. Abel *et al.* (nEDM), Measurement of the permanent electric dipole moment of the neutron, Phys. Rev. Lett. **124**, 081803 (2020), arXiv:2001.11966 [hep-ex].

[5] P. D. Group, P. A. Zyla, R. M. Barnett, J. Beringer, O. Dahl, D. A. Dwyer, D. E. Groom, C. J. Lin, K. S. Lugovsky, E. Pianori, D. J. Robinson, C. G. Wohl, W. M. Yao, K. Agashe, G. Aielli, B. C. Allanach, C. Amsler, M. Antonelli, E. C. Aschenauer, D. M. Asner, H. Baer, S. Banerjee, L. Baudis, C. W. Bauer, J. J. Beatty, V. I. Belousov, S. Bethke, A. Bettini, O. Biebel, K. M. Black, E. Blucher, O. Buchmuller, V. Burkert, M. A. Bychkov, R. N. Cahn, M. Carena, A. Ceccucci, A. Cerri, D. Chakraborty, R. S. Chivukula, G. Cowan, G. D'Ambrosio, T. Damour, D. de Florian, A. de Gouvêa, T. DeGrand, P. de Jong, G. Dissertori, B. A. Dobrescu, M. D'Onofrio, M. Doser, M. Drees, H. K. Dreiner, P. Eerola, U. Egede, S. Eidelman, J. Ellis, J. Erler, V. V. Ezhela, W. Fetscher, B. D. Fields, B. Foster, A. Freitas, H. Gallagher, L. Garren, H. J. Gerber, G. Gerbier, T. Gershon, Y. Gershtein, T. Gherghetta, A. A. Godizov, M. C. Gonzalez-Garcia, M. Goodman, C. Grab, A. V. Gritsan, C. Grojean, M. Grünewald, A. Gurtu, T. Gutsche, H. E. Haber, C. Hanhart, S. Hashimoto, Y. Hayato, A. Hebecker, S. Heinemeyer, B. Heltsley, J. J. Hernández-Rey, K. Hikasa, J. Hisano, A. Höcker, J. Holder, A. Holtkamp, J. Huston, T. Hyodo, K. F. Johnson, M. Kado, M. Karliner, U. F. Katz, M. Kenzie, V. A. Khoze, S. R. Klein, E. Klempt, R. V. Kowalewski, F. Krauss, M. Kreps, B. Krusche, Y. Kwon, O. Lahav, J. Laiho, L. P. Lellouch, J. Lesgourgues, A. R. Liddle, Z. Ligeti, C. Lippmann, T. M. Liss, L. Littenberg, C. Lourengo, S. B. Lugovsky, A. Lusiani, Y. Makida, F. Maltoni, T. Mannel, A. V. Manohar, W. J. Marciano, A. Masoni, J. Matthews, U. G. Meißner, M. Mikhasenko, D. J. Miller, D. Milstead, R. E. Mitchell, K. Mönig, P. Molaro, F. Moortgat, M. Moskovic, K. Nakamura, M. Narain, P. Nason, S. Navas, M. Neubert, P. Nevski, Y. Nir, K. A. Olive, C. Patrignani, J. A. Peacock, S. T. Petcov, V. A. Petrov, A. Pich, A. Piepke, A. Pomarol, S. Profumo, A. Quadt, K. Rabbertz, J. Rademacker, G. Raffelt, H. Ramani,

M. Ramsey-Musolf, B. N. Ratcliff, P. Richardson, A. Ringwald, S. Roesler, S. Rolli, A. Romaniouk, L. J. Rosenberg, J. L. Rosner, G. Rybka, M. Ryskin, R. A. Ryutin, Y. Sakai, G. P. Salam, S. Sarkar, F. Sauli, O. Schneider, K. Scholberg, A. J. Schwartz, J. Schwiening, D. Scott, V. Sharma, S. R. Sharpe, T. Shutt, M. Silari, T. Sjöstrand, P. Skands, T. Skwarnicki, G. F. Smoot, A. Soffer, M. S. Sozzi, S. Spanier, C. Spiering, A. Stahl, S. L. Stone, Y. Sumino, T. Sumiyoshi, M. J. Syphers, F. Takahashi, M. Tanabashi, J. Tanaka, M. Taševský, K. Terashi, J. Terning, U. Thoma, R. S. Thorne, L. Tiator, M. Titov, N. P. Tkachenko, D. R. Tovey, K. Trabelsi, P. Urquijo, G. Valencia, R. Van de Water, N. Varelas, G. Venanzoni, L. Verde, M. G. Vincter, P. Vogel, W. Vogelsang, A. Vogt, V. Vorobyev, S. P. Wakely, W. Walkowiak, C. W. Walter, D. Wands, M. O. Wascko, D. H. Weinberg, E. J. Weinberg, M. White, L. R. Wiencke, S. Willocq, C. L. Woody, R. L. Workman, M. Yokoyama, R. Yoshida, G. Zanderighi, G. P. Zeller, O. V. Zenin, R. Y. Zhu, S. L. Zhu, F. Zimmermann, J. Anderson, T. Basaglia, V. S. Lugovsky, P. Schaffner, and W. Zheng, Review of Particle Physics, Progress of Theoretical and Experimental Physics **2020**, 10.1093/ptep/ptaa104 (2020), 083C01, https://academic.oup.com/ptep/article-pdf/2020/8/083C01/34673722/ptaa104.pdf.

[6] S. Borsanyi *et al.*, Calculation of the axion mass based on high-temperature lattice quantum chromodynamics, Nature **539**, 69 (2016), arXiv:1606.07494 [hep-lat].

[7] M. Dine, P. Draper, L. Stephenson-Haskins, and D. Xu, Axions, Instantons, and the Lattice, Phys. Rev. D **96**, 095001 (2017), arXiv:1705.00676 [hep-ph].

[8] T. Hiramatsu, M. Kawasaki, T. Sekiguchi, M. Yamaguchi, and J. Yokoyama, Improved estimation of radiated axions from cosmological axionic strings, Phys. Rev. D **83**, 123531 (2011), arXiv:1012.5502 [hep-ph].

[9] M. Kawasaki, K. Saikawa, and T. Sekiguchi, Axion dark matter from topological defects, Phys. Rev. D **91**, 065014 (2015), arXiv:1412.0789 [hep-ph].

[10] E. Berkowitz, M. I. Buchoff, and E. Rinaldi, Lattice QCD input for axion cosmology, Phys. Rev. D **92**, 034507 (2015), arXiv:1505.07455 [hep-ph].

[11] L. Fleury and G. D. Moore, Axion dark matter: strings and their cores, JCAP **01**, 004, arXiv:1509.00026 [hep-ph].

[12] C. Bonati, M. D'Elia, M. Mariti, G. Martinelli, M. Mesiti, F. Negro, F. Sanfilippo, and G. Villadoro, Axion phenomenology and $\theta$-dependence from $N_f = 2 + 1$ lattice QCD, JHEP **03**, 155, arXiv:1512.06746 [hep-lat].

32

[13] P. Petreczky, H.-P. Schadler, and S. Sharma, The topological susceptibility in finite tempera-ture QCD and axion cosmology, Phys. Lett. B **762**, 498 (2016), arXiv:1606.03145 [hep-lat].

[14] G. Ballesteros, J. Redondo, A. Ringwald, and C. Tamarit, Unifying inflation with the axion, dark matter, baryogenesis and the seesaw mechanism, Phys. Rev. Lett. **118**, 071802 (2017), arXiv:1608.05414 [hep-ph].

[15] V. B. . Klaer and G. D. Moore, The dark-matter axion mass, JCAP **11**, 049, arXiv:1708.07521 [hep-ph].

[16] M. Buschmann, J. W. Foster, and B. R. Safdi, Early-Universe Simulations of the Cosmological Axion, Phys. Rev. Lett. **124**, 161103 (2020), arXiv:1906.00967 [astro-ph.CO].

[17] M. Gorghetto, E. Hardy, and G. Villadoro, More axions from strings, SciPost Phys. **10**, 050 (2021), arXiv:2007.04990 [hep-ph].

[18] M. Buschmann, J. W. Foster, A. Hook, A. Peterson, D. E. Willcox, W. Zhang, and B. R. Safdi, Dark Matter from Axion Strings with Adaptive Mesh Refinement,  (2021), arXiv:2108.05368 [hep-ph].

[19] J. E. Kim, Weak Interaction Singlet and Strong CP Invariance, Phys. Rev. Lett. **43**, 103 (1979).

[20] M. A. Shifman, A. I. Vainshtein, and V. I. Zakharov, Can Confinement Ensure Natural CP Invariance of Strong Interactions?, Nucl. Phys. B **166**, 493 (1980).

[21] M. Dine, W. Fischler, and M. Srednicki, A Simple Solution to the Strong CP Problem with a Harmless Axion, Phys. Lett. B **104**, 199 (1981).

[22] A. R. Zhitnitsky, On Possible Suppression of the Axion Hadron Interactions. (In Russian), Sov. J. Nucl. Phys. **31**, 260 (1980).

[23] P. Sikivie, Experimental tests of the "invisible" axion, Phys. Rev. Lett. **51**, 1415 (1983).

[24] P. Sikivie, Detection rates for "invisible"-axion searches, Phys. Rev. D **32**, 2988 (1985).

[25] C. Hagmann, D. Kinion, W. Stoeffl, K. van Bibber, E. Daw, H. Peng, L. J. Rosenberg, J. LaVeigne, P. Sikivie, N. S. Sullivan, D. B. Tanner, F. Nezrick, M. S. Turner, D. M. Moltz, J. Powell, and N. A. Golubev, Results from a high-sensitivity search for cosmic axions, Phys. Rev. Lett. **80**, 2043 (1998).

[26] S. J. Asztalos, E. Daw, H. Peng, L. J. Rosenberg, D. B. Yu, C. Hagmann, D. Kinion, W. Stoeffl, K. van Bibber, J. LaVeigne, P. Sikivie, N. S. Sullivan, D. B. Tanner, F. Nezrick, and D. M. Moltz, Experimental constraints on the axion dark matter halo density, The Astrophysical

629    Journal **571**, L27 (2002).

[27]  S. J. Asztalos, R. F. Bradley, L. Duffy, C. Hagmann, D. Kinion, D. M. Moltz, L. J. Rosenberg, P. Sikivie, W. Stoeffl, N. S. Sullivan, D. B. Tanner, K. van Bibber, and D. B. Yu, Improved rf cavity search for halo axions, Phys. Rev. D **69**, 011101 (2004).

[28]  S. J. Asztalos, G. Carosi, C. Hagmann, D. Kinion, K. van Bibber, M. Hotz, L. J. Rosenberg, G. Rybka, J. Hoskins, J. Hwang, P. Sikivie, D. B. Tanner, R. Bradley, and J. Clarke, Squid-based microwave cavity search for dark-matter axions, Phys. Rev. Lett. **104**, 041301 (2010).

[29]  N. Du, N. Force, R. Khatiwada, E. Lentz, R. Ottens, L. J. Rosenberg, G. Rybka, G. Carosi, N. Woollett, D. Bowring, A. S. Chou, A. Sonnenschein, W. Wester, C. Boutan, N. S. Oblath, R. Bradley, E. J. Daw, A. V. Dixit, J. Clarke, S. R. O'Kelley, N. Crisosto, J. R. Gleason, S. Jois, P. Sikivie, I. Stern, N. S. Sullivan, D. B. Tanner, and G. C. Hilton (ADMX Collaboration), Search for invisible axion dark matter with the axion dark matter experiment, Phys. Rev. Lett. **120**, 151301 (2018).

[30]  T. Braine, R. Cervantes, N. Crisosto, N. Du, S. Kimes, L. J. Rosenberg, G. Rybka, J. Yang, D. Bowring, A. S. Chou, R. Khatiwada, A. Sonnenschein, W. Wester, G. Carosi, N. Woollett, L. D. Duffy, R. Bradley, C. Boutan, M. Jones, B. H. LaRoque, N. S. Oblath, M. S. Taubman, J. Clarke, A. Dove, A. Eddins, S. R. O'Kelley, S. Nawaz, I. Siddiqi, N. Stevenson, A. Agrawal, A. V. Dixit, J. R. Gleason, S. Jois, P. Sikivie, J. A. Solomon, N. S. Sullivan, D. B. Tanner, E. Lentz, E. J. Daw, J. H. Buckley, P. M. Harrington, E. A. Henriksen, and K. W. Murch (ADMX Collaboration), Extended search for the invisible axion with the axion dark matter experiment, Phys. Rev. Lett. **124**, 101303 (2020).

[31]  C. Bartram *et al.* (ADMX Collaboration), Search for Invisible Axion Dark Matter in the 3.3–4.2 $\mu$eV Mass Range, Phys. Rev. Lett. **127**, 261803 (2021).

[32]  K. M. Backes, D. A. Palken, S. A. Kenany, B. M. Brubaker, S. B. Cahn, A. Droster, G. C. Hilton, S. Ghosh, H. Jackson, S. K. Lamoreaux, and et al., A quantum enhanced search for dark matter axions, Nature **590**, 238–242 (2021).

[33]  O. Kwon, D. Lee, W. Chung, D. Ahn, H. Byun, F. Caspers, H. Choi, J. Choi, Y. Chong, H. Jeong, J. Jeong, J. E. Kim, J. Kim, i. m. c. b. u. Kutlu, J. Lee, M. Lee, S. Lee, A. Matlashov, S. Oh, S. Park, S. Uchaikin, S. Youn, and Y. K. Semertzidis, First results from an axion haloscope at capp around 10.7 $\mu$eV, Phys. Rev. Lett. **126**, 191802 (2021).

[34]  D. Alesini, C. Braggio, G. Carugno, N. Crescini, D. D'Agostino, D. Di Gioacchino, R. Di Vora,

P. Falferi, U. Gambardella, C. Gatti, G. Iannone, C. Ligi, A. Lombardi, G. Maccarrone, A. Ortolan, R. Pengo, A. Rettaroli, G. Ruoso, L. Taffarello, and S. Tocci, Search for invisible axion dark matter of mass $m_a = 43$ $\mu$eV with the quax–$a\gamma$ experiment, Phys. Rev. D **103**, 102004 (2021).

[35] M. S. Turner, Periodic signatures for the detection of cosmic axions, Phys. Rev. D **42**, 3572 (1990).

[36] M. Lisanti, Lectures on Dark Matter Physics, in *Theoretical Advanced Study Institute in Elementary Particle Physics: New Frontiers in Fields and Strings* (2017) pp. 399–446, arXiv:1603.03797 [hep-ph].

[37] J. Diemand, M. Kuhlen, P. Madau, M. Zemp, B. Moore, D. Potter, and J. Stadel, Clumps and streams in the local dark matter distribution, Nature **454**, 735 (2008), arXiv:0805.1244 [astro-ph].

[38] V. Springel, J. Wang, M. Vogelsberger, A. Ludlow, A. Jenkins, A. Helmi, J. F. Navarro, C. S. Frenk, and S. D. M. White, The Aquarius Project: the subhalos of galactic halos, Mon. Not. Roy. Astron. Soc. **391**, 1685 (2008), arXiv:0809.0898 [astro-ph].

[39] J. F. Navarro, C. S. Frenk, and S. D. M. White, The Structure of cold dark matter halos, Astrophys. J. **462**, 563 (1996), arXiv:astro-ph/9508025.

[40] A. Burkert, The Structure of dark matter halos in dwarf galaxies, Astrophys. J. Lett. **447**, L25 (1995), arXiv:astro-ph/9504041.

[41] G. R. Blumenthal, S. M. Faber, R. Flores, and J. R. Primack, Contraction of Dark Matter Galactic Halos Due to Baryonic Infall, Astrophys. J. **301**, 27 (1986).

[42] O. Y. Gnedin, A. V. Kravtsov, A. A. Klypin, and D. Nagai, Response of dark matter halos to condensation of baryons: Cosmological simulations and improved adiabatic contraction model, Astrophys. J. **616**, 16 (2004), arXiv:astro-ph/0406247.

[43] S. Mashchenko, J. Wadsley, and H. M. P. Couchman, Stellar Feedback in Dwarf Galaxy Formation, Science **319**, 174 (2008), arXiv:0711.4803 [astro-ph].

[44] F. Governato *et al.*, At the heart of the matter: the origin of bulgeless dwarf galaxies and Dark Matter cores, Nature **463**, 203 (2010), arXiv:0911.2237 [astro-ph.CO].

[45] R. H. Dicke, The measurement of thermal radiation at microwave frequencies, Review of Scientific Instruments **17**, 268 (1946), https://doi.org/10.1063/1.1770483.

[46] Y.-H. Chang *et al.*, Taiwan Axion Search Experiment with Haloscope, (2022).

[47] B. Brubaker, L. Zhong, S. Lamoreaux, K. Lehnert, and K. van Bibber, Haystac axion search analysis procedure, Physical Review D **96**, 10.1103/physrevd.96.123008 (2017).

[48] A. Savitzky and M. J. E. Golay, Smoothing and differentiation of data by simplified least squares procedures, Anal. Chem. **36**, 1627 (1964).